Check for updates

Large-Area Semi-Transparent Luminescent Solar Concentrators Based on Large Stokes Shift Aggregation-Induced Fluorinated Emitters Obtained Through a Sustainable Synthetic Approach

Francesca Corsini, Andrea Nitti, Elisavet Tatsi, Giuseppe Mattioli, Chiara Botta, Dario Pasini,* and Gianmarco Griffini*

In this study, the design, fabrication, and characterization of semi-transparent large-area luminescent solar concentrators (LSCs) in thin-film configuration is reported, incorporating a novel organic luminophore (PFPBNT) emitter based on a π-conjugated core flanked by two naphthothiophene units obtained through a chemically sustainable synthetic approach. As found experimentally and validated through computational modeling, PFPBNT exhibits aggregation-induced emission (AIE) behavior, broad absorption in the UV–vis spectrum and significant Stokes shift ($\approx$4632 cm^{-1}), thereby making it an excellent candidate as luminophore in thin-film LSCs based on a poly(methyl methacrylate) (PMMA) matrix, where it is found to show good compatibility, homogeneous distribution, and excellent photostability. After extensive device optimization, PFPBNT/PMMA LSCs with suitable luminophore concentration (12.5 wt%) showed an internal photon efficiency of 17.3% at a geometrical gain of 6.25 under solar-simulated illumination. The size scalability of these systems was also evaluated by means of ray-tracing simulations on devices of up to 1 m^2 surface area. This work demonstrates semi-transparent large-area thin-film LSCs incorporating chemically sustainable AIEgen luminophores, thus opening the way to the development of synthetically affordable, efficient, and stable emitters for the photovoltaic field.

1. Introduction

The integration of high-efficiency photovoltaic (PV) elements in urban areas represents a challenging step toward the achievement of nearly-zero energy architectures.[1] Within this framework, luminescent solar concentrators (LSCs) are a practical and versatile solution for the realization of building-integrated photovoltaics (BIPVs).[2] The idea behind the LSC concept is the replacement of large area PV modules with small solar cells positioned at the edge of a planar monolithic waveguide (e.g., a polymer-based thin-film deposited onto a glass substrate or a bulk plate) containing luminophore species. The luminophores absorb incident sunlight and emit photons which are redirected by total internal reflection toward the thin edges of the waveguide, where the PV elements convert the luminescent light into electricity.[3]

Many different types of luminescent species (e.g., organic fluorophores,[4] perovskite nanocrystals,[5] carbon-dots,[6] and semiconductor quantum dots[7]) have been extensively explored over the past decades in the attempt to achieve a combination of a broad absorption spectrum, a high light-harvesting efficiency, a high solid-state photoluminescence quantum yield (PLQY), and excellent photostability.[8] Nevertheless, the different luminophore- and waveguide-related loss pathways taking place in the LSC[8a,b,9a] still affect the optical performance of current systems and represent important obstacles to the sustainable commercialization of this technology.

F. Corsini, E. Tatsi, Prof. G. Griffini
Department of Chemistry
Materials and Chemical Engineering "Giulio Natta"
Politecnico di Milano
Piazza Leonardo da Vinci 32, Milano 20133, Italy
E-mail: gianmarco.griffini@polimi.it

The ORCID identification number(s) for the author(s) of this article can be found under https://doi.org/10.1002/adom.202100182.

Dr. A. Nitti, Prof. D. Pasini
Department of Chemistry and INSTM Research Unit
University of Pavia
Viale Taramelli 10, Pavia 27100, Italy
E-mail: dario.pasini@unipv.it

Dr. G. Mattioli
CNR – Istituto di Struttura della Materia
Area della Ricerca di Roma
Monterotondo Scalo I-00015, Italy

Dr. C. Botta
Institute of Sciences and Chemical Technologies "Giulio Natta" (SCITEC) of CNR
via Corti 12, Milano 20133, Italy
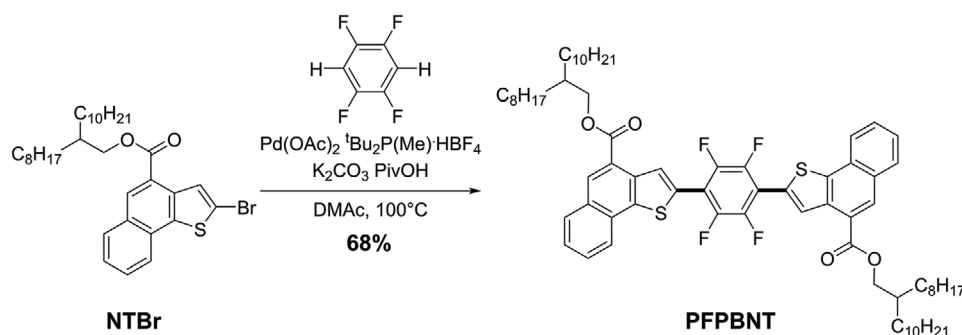
Scheme 1. Synthesis of PFPBNT

In this context, two of the main problems associated with the most popular organic luminophores are their aggregation-caused luminescence quenching (ACQ) and their small Stokes' shift that promote self-absorption processes when the re-emitted light traverses the waveguide.[9b] Both phenomena strongly reduce the light output and limit the efficiency of most of the current LSC devices. Many strategies have been proposed to overcome ACQ.[8a,b,9a] Among these, aggregation-induced emission luminogens (AIE*gens*) have recently opened new avenues in solid-state emissive devices.[10] Typical AIE*gens* possess propeller-like or rotor structures able to avoid the formation of close π–π stacking in the solid-state and thus suppress the major cause of non-radiative decay, favoring the emission processes.[11] The first application of an AIE*gen* in lab-scale small-area LSC systems[10d] was based on the dispersion of tetraphenyl–ethylene in a PMMA thin film. Despite the promising PLQY value of 41%, the absorption centered in the near-UV range and the fluorescence in the blue wavelength range strongly limited the maximum achievable power conversion efficiency (PCE). After that, several papers have reported on the use of AIE*gens* as single dyes in LSCs,[12] or combined with other dyes in order to achieve Förster resonance energy transfer (FRET),[13] limiting the investigations to lab-scale devices.

From a synthetic chemistry perspective, the introduction of fluorine atoms into the skeleton of conjugated backbone has led to an impressive variety of functionalized organic semiconductors applied in devices.[14] Fluorine functionalization increases thermal and oxidative stability, influences optoelectronic properties (fluorine resonance electron-donating effects generally lower the HOMO energy with minor effects on the LUMO energies) and steric interactions (the small atomic radius of fluorine significantly influences the molecular organization in the condensed state). In addition, fluorine substitution has an influence on the molecular packing, promoting specific noncovalent interactions which can yield semicrystalline, more ordered materials, with important consequences related to their optoelectronic performance and, in particular, to their AIE activity. Indeed, fluorine functionalization has been extensively used for the synthesis of solid-state luminophores in past years.[15]

Based on these considerations, semi-transparent large-area thin-film LSCs incorporating chemically sustainable AIE*gen* luminophores were demonstrated and presented in this work. The new large-Stokes-shift AIE system presented here (referred to as PFPBNT hereon) features a tetrafluorobenzene central core end-capped with naphthothiophenes,[16] and was obtained through a low E-factor (i.e., the ratio of the mass of waste and the mass of product) synthetic process based on recently developed eco-friendly direct heteroarylation (DHA) and Suzuki cross-coupling methodologies demonstrated by our group[17] and in literature for optically-active materials.[18]

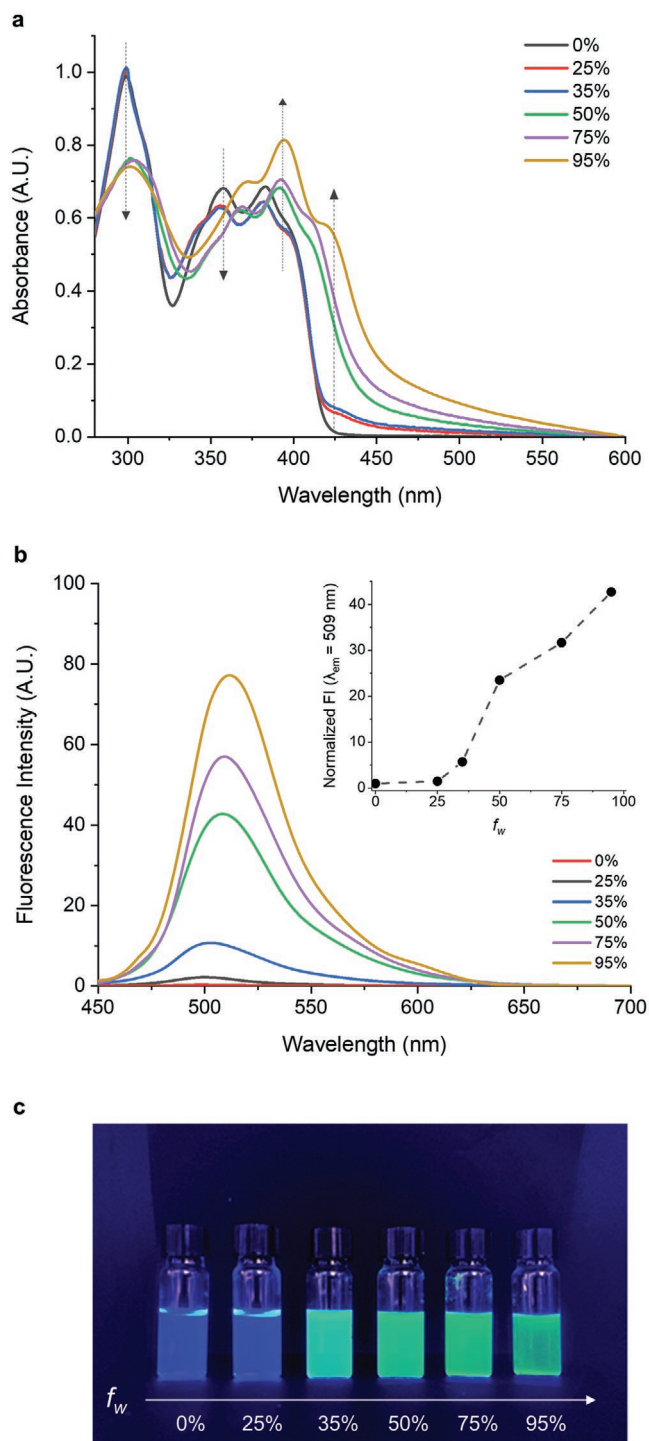## 2. Results and Discussion

2.1. Synthesis of PFPBNT

The reaction route for the synthesis of PFPBNT is shown in **Scheme 1**. The synthesis of PFPBNT is the result of the DHA between a commercially available 1,2,4,5-tetrafluorobenzene (TFB) and a naphthothiophene derivative NTBr using $Pd(OAc)_2$ and $^tBu_2P(Me) \cdot HBF_4$ as catalytic system, K_2CO_3 as base, PivOH as additive in DMAc at 100 °C. The DHA protocol reported in Scheme 1 refers to the best reaction condition obtained from an extensive screening of Pd-catalysts, phosphine, bases, solvent, and reaction temperatures (see Table S1, Supporting Information). NTBr was obtained in two steps with a protocol reported in literature.[16]

The sustainability factor (E-factor) of the synthetic process was calculated as shown in Table S1, Supporting Information. An E-factor as low as 99 was achieved, that is a value ten times lower than conventional LSC emitters (e.g., the synthesis of Lumogen F Red 305, the prototypical LSC molecular dye, has been estimated to have an E-Factor > 1000),[19] thus demonstrating the enhanced chemical sustainability of the synthetic methodology adopted in this work.

2.2. Aggregation-Induced Emission (AIE) Property of PFPBNT

The AIE property of PFPBNT was investigated by focusing on its UV absorption and photoluminescence (PL) emission behavior when diluted in THF-H_2O mixtures with different volume fractions of water (f_w).

As depicted in **Figure 1**a, PFPBNT in pure THF displays a fine-structure absorption spectrum with three absorption bands centered at 298, 362, and 385 nm, respectively. These absorption peaks could be assigned to the π–π* transition of the whole conjugated π-electron system. As the f_w value in THF–H_2O mixtures was increased, the maximum absorption peak at 298 nm

**ADVANCED
SCIENCE NEWS**
www.advancedsciencenews.com

**ADVANCED
OPTICAL
MATERIALS**
www.advopticalmat.de

Figure 1. a) UV–vis spectra of dilute solutions of PFPBNT (9.5×10^{-6} M) in THF–H$_2$O mixtures with different volume fractions of water (f_w = 0%, 25%, 35%, 50%, 75%, and 95%). b) Steady-state fluorescence spectra for 2.5×10^{-4} M PFPBNT in THF–H$_2$O mixtures at different f_w values (λ_{exc} = 412 nm). The inset shows the normalized PL intensity at λ_{em} = 509 nm as f_w changes. c) Photographic image of THF–H$_2$O mixtures at different f_w ratios under 365 nm UV light.

diminished, together with the one at 362 nm. Meanwhile, a new shoulder appeared at ≈423 nm with an absorption intensity increasing continuously with f_w. Also, the peak at 385 nm

was found to increase and shift to longer wavelengths and level-off tails in the visible region were detected for f_w > 25%, demonstrating the onset of the formation of aggregates. Such tails were attributed to the Mie scattering effect,[20] which is commonly observed in nanoparticle suspensions.

PL spectra of $2.5 \ 10^{-4}$ M PFPBNT in THF–H$_2$O mixtures with varying f_w are shown in Figure 1b. PFPBNT in pure THF and in mixtures with f_w < 25% exhibited weak PL emission. In fact, the solutions showed weak bluish emission under 365 nm UV illumination (see Figure 1c). Conversely, when f_w reached 35%, a green emission was observed with λ_{max} = 509 nm, whose intensity was found to sharpen considerably by further increasing water content. The emission intensity for f_w = 95% was more than 40 times higher than the intensity in pure THF (see insert in Figure 1b). While the blue emission in pure THF displayed a very fast mono-exponential decay (τ = 538 ps, λ_{exc} = 300 nm, λ_{em} = 412 nm), the green emission of the THF–H$_2$O mixtures showed slow bi-exponential decays (τ = 3.29 ns, λ_{exc} = 408 nm, and λ_{em} = 513 nm for f_w = 95%). This observation confirms the presence of vibrational and rotational quenching channels in the pure THF solution, that are suppressed in the green emissive solutions thanks to the restricted intramolecular motions induced by nanoaggregation. These spectral changes and the very strong green fluorescence under 365 nm UV illumination (for f_w > 25%) clearly demonstrate the aggregation-induced green emission of PFPBNT. The formation of highly emissive aggregated particles, attributed to the intrinsic hydrophobic nature of the AIE molecule,[21] was further confirmed by fluorescence microscopy (Figure S3, Supporting Information).

The UV–vis absorption and PL response of PFPBNT was also evaluated when deposited in thin-film form. In particular, the UV–vis and PL spectra profiles and emission decay dynamics were found to be similar to those observed in high-f_w THF–H$_2$O solutions, while bathochromically shifted (**Figure 2**; and Figure S5, in the Supporting Information). Conversely, a two-fold increase in PLQY was observed with respect to the solution as the inset of Figure 2 shows.

2.3. Optoelectronic Properties of PFPBNT by Atomistic Simulations

Structural, electronic, and optical properties of PFPBNT and of its aggregates were investigated by tight-binding and ab initio atomistic simulations, in order to shed light on the photophysical and structural characteristics discussed in the previous sections. As illustrated in **Figure 3**, long alkyl tails were trimmed shorter to reduce the computational cost, without compromising the relevance of the investigated structures. The most significant structural feature of an isolated molecule is represented by its twisted geometry (green arrow in Figure 3a), with the fluorinated core forming a solid angle of ≈30° with the planes of the side naphthothiophene units. Optical properties of aggregates stem from such twisted geometry, as discussed below. Frontier orbitals calculated by using the B3LYP functional are also shown in Figure 3; both orbitals are generally distributed across the whole π-conjugated system, with the HOMO involving the donor naphthothiophene units to a greater extent, and the LUMO more localized on the acceptor fluorinated core and on the −COOR moieties. Absorption and emission spectra
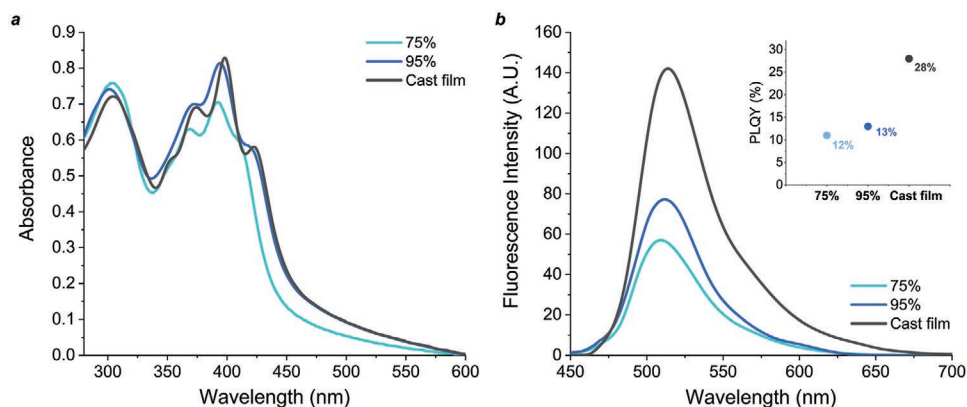
Figure 2. a) UV–vis and b) fluorescence spectra of PFPBNT thin films and THF–H_2O mixtures with high water fraction f_w ($\lambda_{ex} = 412$ nm).

of an isolated PFPBNT were calculated using TDDFT and compared with results obtained in the case of the most stable dimer. Trends can be extrapolated from such results, which are useful for the interpretation of the AIE features discussed in the previous section on the grounds of experimental results. Vibrationally resolved absorption and fluorescence spectra of PFPBNT are shown in Figure 3b. A strong $S_0 \rightarrow S_1$ transition, falling at 393 nm and basically corresponding to a one-electron HOMO→LUMO transition, dominates the near-UV spectrum of the molecule with its vibrational progression. The difference in electronic density between excited and ground states is shown in the figure inset, suggesting displacement of charge (highlighted by black arrows) from blue regions in side units to red regions in the central core and −COOR moieties upon excitation of the molecule. At lower wavelength (356 nm), a weaker dipole-allowed $S_0 \rightarrow S_3$ transition modulates the shape of the band and can lead to slight variations in the position of the apparent maxima of the spectrum in the near UV region, making a close comparison with experimental data highly dependent on the TDDFT exchange-correlation kernel used for the simulations. The corresponding calculated fluorescence (dashed curve in Figure 3b) predicts a sizable Stokes' shift (7640 cm^{-1}), suitable for LSC applications. A tendency to the reduction of the solid

angle between the planar core and side units is suggested by an accumulation of π-charge on the C−C single bonds, marked by red arrows in the inset to Figure 3b. An enhancement of the double-bond character of such C−C bonds leads to the significant planarization of the molecule in the S_1 state (confirmed by geometry optimization of the excited state), which extends the conjugation of the molecule and is compatible with a red shift of fluorescence, as already observed in the case of oligothiophene molecules.[22] Minimum energy configurations of two and four PFPBNT molecules found by applying the CREST algorithm indicate that PFPBNT molecules tend to aggregate forming stacks, in which each molecule retains the twisted structure of the monomer, and the alkyl tails work as alternate, interlocking bodies that hinder the intramolecular rotation of aromatic rotors observed in the case of the isolated molecule. Normalized absorption spectra of monomer and dimer, together with electronic transitions and the corresponding oscillator strength, are shown in Figure 3c. Aggregation, even limited to two molecules, displays the same trend shown by measurements as indicated by dashed arrows in the figure. More specifically, a red shift of the absorption onset is accompanied by a weakening of the band peaked at ≈300 nm. It is worth noting that the somewhat surprising red shift of the onset does not agree
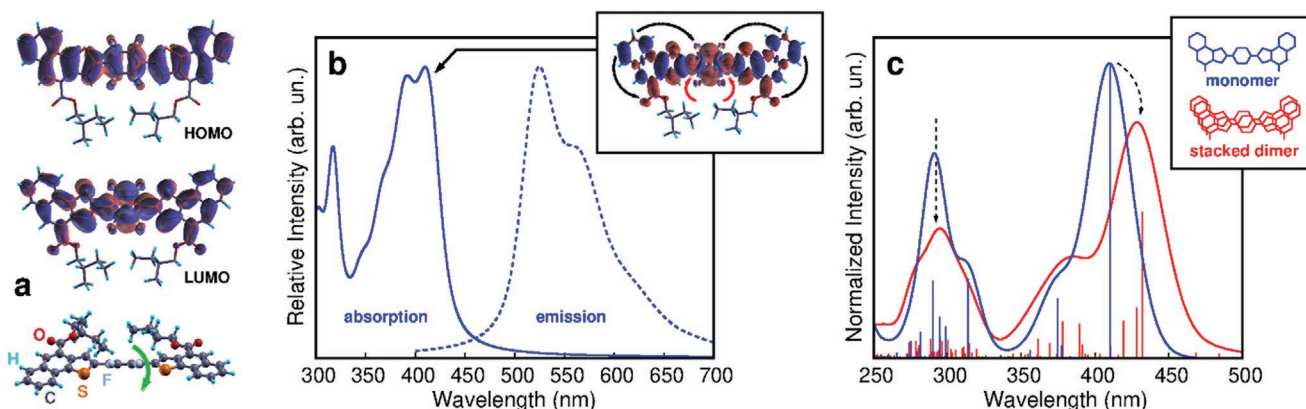
Figure 3. a) Optimized geometry and isosurfaces of HOMO and LUMO orbitals of an isolated PFPBNT molecule. b) Vibrationally resolved TDDFT absorption and fluorescence spectra of PFPBNT; charge displacement from blue regions to red regions accompanying the $S_0 \rightarrow S_1$ transition is shown in the inset. c) TDDFT absorption spectra, obtained as Gaussian ($\sigma = 2000$ cm^{-1}) convolutions of electronic transitions, reported as bars proportional to the oscillator strength in the same panel, of a PFPBNT molecule (blue) and of a stacked dimer (red).
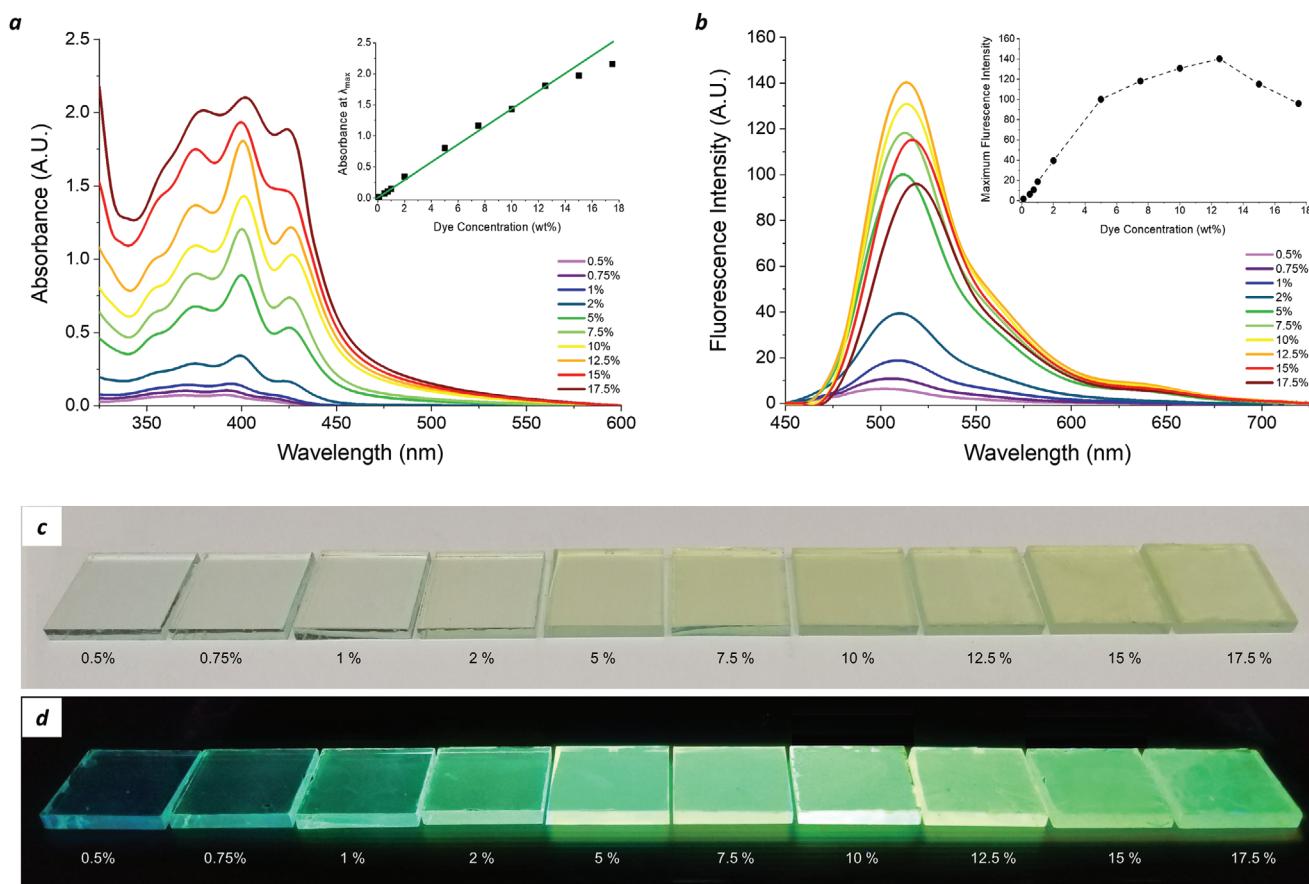
Figure 4. Optical properties of PFPBNT/PMMA coatings. a) UV–vis absorption spectra and b) emission spectra (λ_{exc} = 412 nm) of PFPBNT/PMMA samples as a function of luminophore concentration (wt%). In the insets, the absorbance/fluorescence maximum was plotted as a function of the AIE*gen* species content. Photographs of PFPBNT/PMMA LSC systems (5.0 × 5.0 × 0.6 cm^3) with varying concentrations of PFPBNT c) under daylight conditions and d) under 365 nm UV light.

with the predictions of the Frenkel–Davydov excitonic model to molecular aggregates,[23] which suggests blue-shift of absorption in cofacial aggregates of π-conjugated molecules. Simulations, on the whole, suggest that the conformational flexibility of the isolated molecule is responsible for its low fluorescence yield in THF solution, as the coupling of the electronic excited state with nuclear motion provides a preferential, non-radiative path to the ground state. Aggregation leads instead to the formation of stacks in which rotation is hindered, enhancing the emissive properties of the molecules.[11b]

2.4. Photophysical Characterization of PFPBNT/PMMA-Based LSCs

As previously demonstrated in literature, the aggregation of AIE*gens* can be stimulated not only by introducing a poor solvent in solution, but also by forcing them to pack in a solid matrix.[12] Accordingly, considering its AIE property, its broad absorption and its relatively large Stokes shift (≈4632 cm^{-1}), PFPBNT was investigated as luminophore species for LSC devices in thin-film configuration.

Control over the dye concentration is essential for achieving intrinsically high efficiency in LSCs.[24] Therefore, we analyzed

the absorption and PL spectra of PFPBNT embedded in PMMA as host matrix at various concentrations (0.5–17.5 wt%) (**Figure 4**).

As evident from the plots in Figure 4b, the PL intensity sharply increased up to a luminophore concentration in PMMA of 5 wt%, followed by a steady but more moderate growth for higher PFPBNT loading (up to 12.5 wt%). Such two-step behavior could be attributed to a faster increase in the probability of occurrence of reabsorption events for higher (>5 wt%) luminophore concentrations. At concentrations higher than 12.5 wt%, a fast attenuation of PL intensity was recorded, accompanied by a slight (6 nm) red-shift in the emission peak, probably due to reabsorption and self-absorption phenomena.[12c,25] Another plausible cause of such PL intensity weakening could be the limited solubility of the AIE*gen* into the host matrix at high concentrations. As previously reported,[12d,13a,b] for high concentration, the dye molecules swiftly agglomerate in a random way to form both less emissive amorphous supramolecular aggregates and scattering sites. These phenomena match well with the deviation from linearity observed on the experimentally determined absorbance at high dye concentrations (see inset to Figure 4a). The optimal threshold value of 12.5 wt% does not have precedent in literature and, to our knowledge, represents the highest AIE*gen* luminophore loading reported in LSC devices to date. Also, the
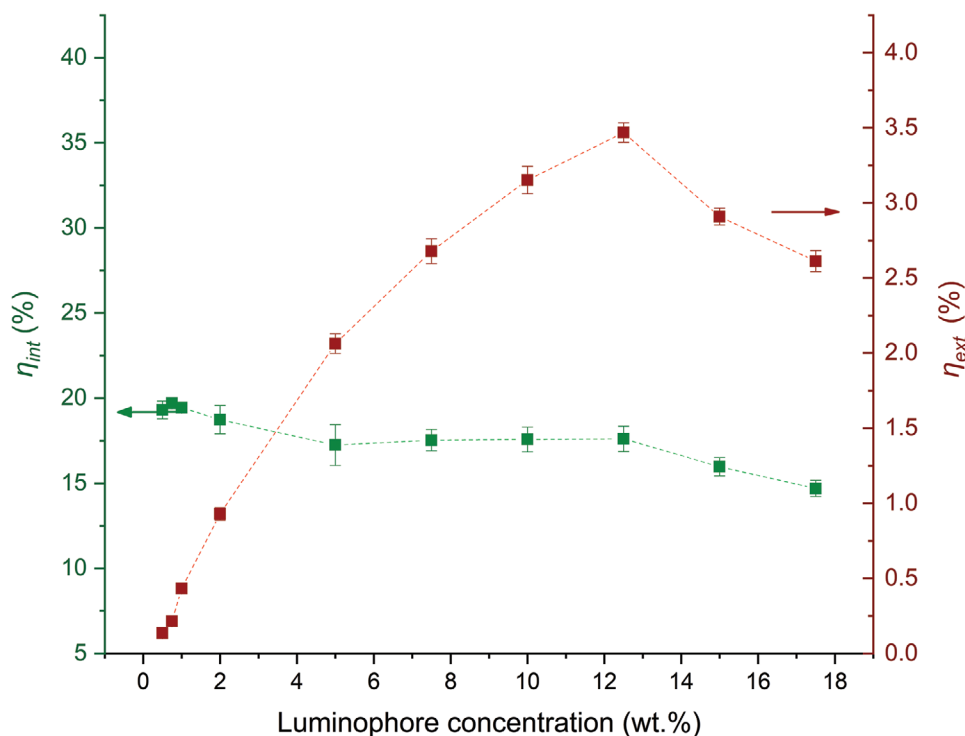
Figure 5. Internal and external photon efficiency (η_{int} and η_{ext}, respectively) versus luminophore concentration. The corresponding values are listed in Table S3, Supporting Information.

PLQY of PFPBNT at different luminophore concentrations was measured to compare the emission intensities. As more extensively discussed in Section S10, Supporting Information, the trend of PLQY values is in good agreement with that illustrated in **Figure 5**. The absorption efficiency (η_{abs}) and the radiative overlap (*RO*) of LSC systems as a function of the luminophore doping level were also estimated, according to Equations (S1) and (S2), Supporting Information. Even though limited η_{abs} values could be reached by PFPBNT/PMMA-based systems due to the partial overlap between PFPBNT absorption and solar emission spectra, for similar η_{abs} values, the portion (%) of reabsorbed photons (associated to *RO*) in PFPBNT resulted to be remarkably lower than in many commercial organic dyes (e.g., Lumogen F Red 305).[26] These evidences further suggest the viability of PFPBNT as promising candidate luminophore for large-area LSC devices.
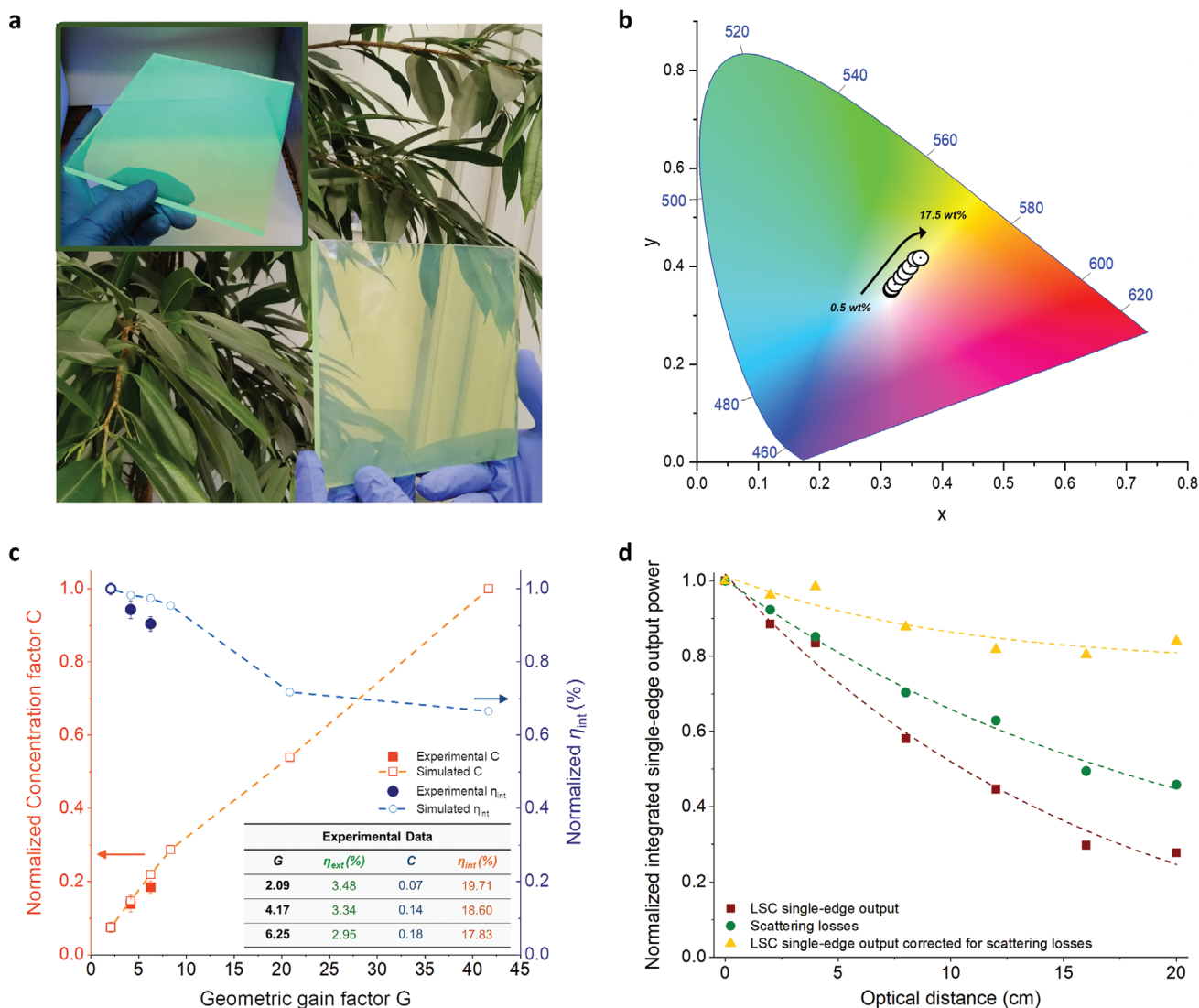
2.5. Experimental Evaluation of PFPBNT/PMMA-Based LSC Performance and Monte Carlo Ray-Tracing Modeling

In order to validate the potential of PFPBNT/PMMA-based systems for LSCs in thin-film configuration, both the external photon efficiency (η_{ext}) and the internal photon efficiency (η_{int}) were assessed under standard illumination conditions (AM 1.5G). η_{ext} and η_{int} were calculated from the experimental data according to Equations (S4) and (S5), Supporting Information.[27]

As shown in Figure 5, up to a concentration of 12.5 wt%, a relatively constant η_{int} was observed (≈18%), followed by a slight decrease at the higher luminophore loadings. As concerns η_{ext}, its highest value (≈3.5%) was achieved for PFPBNT loading equal to 12.5 wt%, in agreement with the photophysical response of this system previously discussed. The decrease in η_{ext} after this threshold concentration may suggest the occurrence of detrimental self-absorption phenomena as well as the generation of scattering losses, as previously mentioned. As a matter of fact, the efficiency of the PFPBNT/PMMA LSC could be critically limited by the formation of a great amount of large PFPBNT aggregates in the PMMA host matrix at high concentrations, which may induce both reabsorption and scattering losses. The occurrence of the latter loss mechanism at the highest concentrations was evident in the UV–vis spectra of PFPBNT/PMMA systems with high loading level (Figure 4a), where level-off tails in the long wavelength region were detected. This was accompanied by a significant increase in opaqueness/scattering of the samples, as clearly visible upon inspection under daylight conditions (Figure 4c).

On the basis of the results above, large-area (10.0 × 10.0 × 0.6 cm³ and 15.0 × 15.0 × 0.6 cm³) PFPBNT/PMMA LSC devices with optimized luminophore concentration (12.5 wt%) were fabricated using a doctor-blade deposition technique. A prototype of semi-transparent large-area LSC is depicted in **Figure 6**a. Colorimetry analysis of LSC systems at increasing PFPBNT concentration were performed to assess the parameter of transmitted light and to quantify the color perception of PFPBNT/PMMA LSC devices in working conditions. Specifically, the color of the LSCs was evaluated using the Commission Internationale de l'Eclairage (CIE) *L*a*b** color space, which is the conventional approach for assessing the visual appearance of

ADVANCED
SCIENCE NEWS
www.advancedsciencenews.com

ADVANCED
OPTICAL
MATERIALS
www.advopticalmat.de

Figure 6. a) Photographs of a PFPBNT/PMMA LSC (dimensions of $15 \times 15 \times 0.6$ cm³, soda-lime glass substrate) under UV-A and ambient illumination light. b) Color coordinates (CIE 1931 Uniform Color Space) of PFPBNT/PMMA LSC systems at increasing luminophore concentration. c) C and η_{int} as a function of G for optimized PFPBNT/PMMA LSCs. The solid symbols represent the experimental results, whereas the hollow symbols represent the simulated values. In the inset: table reporting the experimental values for η_{ext}, C and η_{int} at increasing G. d) Normalized intensity decay of the integrated optical power output as a function of optical distance from the illumination spot under 1 sun top illumination (red squares) and under irradiation using a 655 nm light (green circles). The calculated integrated optical power output corrected for scattering losses (orange triangles) is also shown. The dashed lines represent an exponential fit to the data.

materials under standard illumination. As can be noticed in Figure 6b, the transmitted light presented CIE color coordinates of $x = 0.335$ and $y = 0.346$, color-rendering index (CRI) of 96.88 and correlated color temperature (CCT) = 5395 K at a luminophore concentration of 0.5 wt%, clear evidence of the excellent transparency of the considered LSC systems at low dye doping levels. A considerable transparency was displayed even from highly concentrated LSC devices (e.g., with 17.5 wt%), which resulted to be characterized by CIE color coordinates of $x = 0.379$ and $y = 0.410$, CRI of 87.91 and CCT = 4295 K at high luminophore concentration.

To evaluate the optical performance of PFPBNT/PMMA LSCs, η_{ext}, optical concentration factor ($C = \eta_{ext} \cdot G$) and η_{int}

as a function of the geometrical gain G were experimentally determined. At $G = 2.09$ (corresponding to the 5×5 cm² LSC device), η_{ext}, C and η_{int} resulted to be equal to 3.48%, 0.076%, and 19.71%, respectively. When increasing G, a progressive increase in C was observed accompanied by a decrease in η_{int} (see Figure 6c), likely ascribable to the occurrence of different types of losses (e.g., reabsorption, scattering, and waveguide light transport) in PFPBNT/PMMA LSC during the propagation of the emitted light from the device center to edges. For 15×15 cm² LSC systems (i.e., $G = 6.25$), η_{ext}, C, and η_{int} reached values of 2.95%, 0.18, and 17.83%, respectively.

Ray-tracing simulations were also conducted for the validation of the experimental observations and for predicting the

optical response on larger scale LSCs (see Section S.11, Supporting Information, for details). In analogy with the experimental architecture, calculations were performed on squared thin-film devices with fixed glass substrate and coating thickness ($t_1 = 0.6$ cm and $t_2 = 0.002$ cm, respectively) and varying lateral dimension ($l = 5$–100 cm) under standard illumination (AM 1.5G) and employing 1'000'000 incident rays. The results of the simulations for C and η_{int} as a function of G for the six cases considered ($l = 5$, 10, 15, 20, 50, and 100 cm, corresponding to $C = 2.09$, 4.17, 6.25, 8.33, 20.83, 41.67) are reported in Figure 6c. When increasing G at constant device thickness, C was found to steadily increase, as opposed to the moderate (33%) decrease observed in η_{int} when moving from small-scale (5 × 5 cm^2, $G = 2.09$) to 1 m^2 ($G = 41.67$) LSCs. In agreement with the experimental outcomes, the intensity of the simulated single-edge spectra was found to progressively decrease with device size enlargement. Furthermore, a progressive bathochromic shift in the edge-emission maximum was observed by increasing device size (Figure S10, Supporting Information). These trends can be associated to the increase in number of reabsorption and scattering events together with the appearance of waveguiding transport losses with increasing G, and appear to be fully in line with the results obtained on fabricated PFPBNT/PMMA devices reported in Figure 6 ($G = 2.09$–6.25), indicating excellent match between simulation and experimental data.

To experimentally evaluate the contribution of such optical losses, the single-edge optical output power spectrum for the LSC as a function of the optical pathlength d between the excitation spot and the collecting edge was recorded (Figure S11, Supporting Information). For this test, high-optical-quality N-BK7 glass (with absorption coefficient $\alpha = 10^{-3}$ cm^{-1}) was used as waveguide, thus allowing the minimization of waveguide light transport losses.[2a,28] As the optical distance from the collecting edge increased, the single-edge optical output power was found to progressively decrease. Also, a small red shift in the emission maximum was observed (see Figure S11b, Supporting Information). These trends could in principle be ascribed to the simultaneous occurrence of reabsorption and scattering losses. In particular, to isolate the contribution of scattering losses, the optical edge output was also monitored as a function of the optical distance by illuminating the top surface of the LSC with a monochromatic light centered at 655 nm. Since PFPBNT does not absorb at this wavelength (Figure 4a), any losses recorded in the optical output power can be attributed in this case to scattering events. As can be observed in Figure 6d (green squares), scattering losses are indeed responsible for a great part of the decrease in output power, with a reduction of ≈50% at an excitation distance from the collecting edge of 20 cm. This is an intrinsic issue of AIE*gen*-based LSC systems, since the scattering phenomenon is ascribable to the existence of the luminophore in the form of highly emissive molecular aggregates within the host matrix.[13a] Knowing the contribution from photon scattering losses, the net effect of reabsorption losses could therefore be isolated at a given optical distance, as shown in Figure 6d. As expected, given the negligible overlap between the PFPBNT absorption and PL spectra, only a minor decrease in optical output power as a function of d could in fact be associated to photon reabsorption issues (≈10% at optical distances up to 20 cm).

2.6. Photovoltaic Characterization of PFPBNT/PMMA LSC-PV Assembly

To assess the performance of the assembled LSC-PV system with optimum AIE*gen* concentration (12.5 wt%), photocurrent measurements were accomplished after coupling two c-Si PV modules to two opposite edges of the LSC as described in the Experimental Section. The power conversion efficiency (η_{dev}) was determined by means of PV measurements (Equation (S6), Supporting Information). The tests were carried out in the presence of either a black absorbing background or a white scatterer, as more precisely described in the Experimental Section. The complete collected data (V_{OC}, I_{SC}, FF, P_{max}, and η_{dev}) are reported in Table S5 and Figure S12, Supporting Information. For PFPBNT/PMMA LSC-PV assembly with the optimized luminophore concentration, a maximum I_{SC} of 4.45 mA and a maximum output power (P_{max}) of 4.75 mW were achieved, leading to a maximum overall (four edges) η_{dev} as high as 0.38%. Moreover, it is interesting to note the significant impact of the experimental configuration on the performance of PFPBNT/PMMA LSC devices. In accordance with previous studies,[29] the value of overall η_{dev} in the presence of a white scatterer at the rear side of the LSC resulted in an ≈20% performance improvement with respect to the black absorbing background condition. Indeed, back scattering and reflection of otherwise lost unabsorbed light contribute significantly to enhance LSC performance. The relatively small values of η_{dev} obtained with both configurations are justified by the non-optimized matching between the absorption spectrum of the luminophore and the solar emission spectrum (i.e., η_{abs}, Figure S7, Supporting Information), and by the non-optimized overlap between the spectral response of the PV cell and the emission spectrum of the luminophore specie. Nevertheless, such performance is in line with LSCs incorporating luminophores with similar optical response (absorption and emission) and recently reported in the literature,[6a,12c,30] thus confirming the potential of this AIE*gen* scaffold as efficient luminescent species for LSC applications.

Finally, the long-term photostability of PFPBNT/PMMA-based LSCs were also assessed in view of their envisaged use in BIPV. By monitoring the optical performance of optimized devices over time under white-light illumination (see Experimental section; and Figure S12, Supporting Information), excellent preservation of the initial LSC response was recorded even after more than 80 h of continuous light-exposure in air, further demonstrating the application potential of this novel AIE*gen*-based luminescent system.

3. Conclusion

In summary, we have demonstrated the design, fabrication, and characterization of semi-transparent large-area LSCs in thin-film configuration incorporating a novel organic AIE luminophore (PFPBNT) characterized by large Stokes shift and obtained through a chemically sustainable (low E-factor) synthetic approach. By optimizing the concentration of PFPBNT in PMMA, the LSC system was found to exhibit a maximum η_{ext} of 3.46% and a maximum η_{int} of 17.95% under simulated

sunlight illumination (1000 W m^{-2}). The performance was found to scale with the size of the LSC device, as demonstrated by ray-tracing simulations on systems of up to 1 m^2 active area. In addition, the integrated PFPBNT/PMMA-based LSC system displayed excellent photostability as inferred from long-term (>80 h) continuous white-light illumination exposure experiments in air.

In view of the intrinsically sustainable synthetic procedure employed to obtain PFPBNT displaying an E-factor value significantly lower than conventional luminophores currently used in the LSC field, the limited reabsorption losses afforded by its large Stokes shift, and the performance and excellent stability of the resulting PFPBNT/PMMA-based devices, our findings provide a direct demonstration of the application potential of this system as large-area, efficient, and stable semi-transparent LSCs.

4. Experimental Section

Materials: All commercially available reagents and solvents were purchased from Sigma–Aldrich, Fluorochem, TCI, and Alfa Aesar. They were all used as received. PMMA (ALTUGLAS BS 550) and index matching liquid 150 (IML150) were purchased from Arkema and Norland, respectively. Compounds naphtho[1,2-*b*]thiophene and benzo[1,2-*b*:6,5-*b'*] dithiophene 4-carboxylate esters bearing 2-octyldodecyl side chains were synthesized according to literature.[31] Flash chromatography was carried out using Merck silica gel 60 (pore size 60 Å, 270–400 Mesh). Monocrystalline high efficiency silicon solar cells were provided by IXYS (IXOLAR SolarBIT KXOB22-12 × 1F, active area 2.2 × 0.6 cm^2, V_{OC} = 0.64 ± 0.01 V, J_{SC} = 42.60 ± 0.42 mA cm^{-2}, FF = 69.4 ± 0.3%, power conversion efficiency = 18.69 ± 0.23%).

Measurements: ^{1}H and ^{13}C NMR spectra were recorded from solutions in deuterated solvents on 400 Jeol with tetramethylsilane as internal standard. Mass spectra of pure compounds were recorded using a Bruker Autoflex MALDI-TOF in positive reflectron mode with trans-2-(3-(4-tert-Butylphenyl)-2-methyl-2-propenylidene)malononitrile (DCTB) as a matrix. Hermogravimetric analysis (TGA) was performed using a TA Instruments Q500 thermogravimetric analyser. Measurements were carried out in air from 25 °C to 800 °C, with a constant heating rate of 10 °C·min^{-1} and using ≈15 mg of PFPBNT sample placed in a ceramic crucible. Differential scanning calorimetry (DSC) analyses were performed with a DSC 823e Mettler–Toledo instrument. The samples of ≈8 mg were subjected to a thermal cycle from 30 °C to 200 °C with heating rate of 10 °C·min^{-1}. Micrographs of PFPBNT nanoaggregates were captured through a Leica DMI3000B fluorescence microscope equipped with a digital camera, by using specific filters based on the excitation and emission wavelengths of the investigated sample. Photoluminescence quantum yield of PFPBNT in THF–H$_2$O mixtures with water fraction (f_w) equal to 95%, of PFPBNT in solid state and of PFPBNT/PMMA coating with optimized concentration (12.5%) were measured with a home-made integrating sphere according to the procedure reported elsewhere.[32] Fluorescence time-resolved TCSPC measurements were performed with a NanoLog composed of a iH320 spectrograph equipped with a PPD-850 single photon detector module and a DeltaTime series DD-405L DeltaDiode Laser and analysed with the instrument software DAS6. UV–vis absorption spectra were recorded on a Thermo Scientific Evolution 600 UV–vis spectrophotometer using wavelength scan with a resolution of 1 nm at a scan speed of 120 nm min^{-1} and a slit width of 2 nm. Steady-state fluorescence spectroscopy analyses were performed on a Jasco FP-6600 spectrofluorometer. Photoluminescence (PL) spectra of PFPBNT/PMMA samples were recorded in front-face emission configurations and the excitation and emission slits were adjusted so that the maximum emission intensity was within the range of linear response of the detector. Internal and external photon efficiency (η_{int}

and η_{ext}, respectively) measurements were performed by illuminating the top face of the LSC using a Abet Technologies Sun 2000 solar simulator with AM1.5G filter (irradiance of 1000 W·m^{-1}) and by collecting the edge emission of the LSC devices with a spectroradiometer (International Light Technologies ILT950) equipped with a cosine corrector. The emission spectra of the LSCs were recorded using Spectrilight software. A digital multimeter (KEITHLEY 2612B) was connected in series with the circuit, between the PV module and the potentiometer, to perform the voltage scans and measure the current output. PV tests were repeated both by placing an absorbing black background in contact with the LSC rear side to avoid photocurrent overestimation due to photon double-pass effects, and by fixing a white diffuser (Edmund Optics, #34-480) in contact with the back surface of the LSC to allow back scattering of transmitted photons. In both experimental setups, a black mask placed on the front face of the LSC system was used to avoid direct illumination of the PV cells. These photocurrent measurements allowed to determine the device efficiency of LSC-PV assembly. All the above cited tests were repeated for at least three devices.

The PFPBNT/PMMA coating with optimized concentration was subjected to weathering tests under continuous Xenon light illumination and aerobic conditions. The total irradiance was measured with the spectroradiometer and set at approximately 1000 W·m^{-2} (600 W·m^{-2} in the 300–800 nm wavelength range and 12 W·m^{-2} in the 295–400 nm range) for the entire duration of the test. The relative humidity and the working temperature inside the testing chamber were maintained constant and measured to be 35% and 45 °C, respectively. The normalized trend for integrated single-edge optical power output was calculated by dividing the value measured at a given exposure time by the value measured at 0 h of exposure.

Accelerated aging tests were also performed in combination with UV–vis and fluorescence spectroscopy to assess the photostability of the PFPBNT in THF–H$_2$O mixture with f_w equal to 75% under UV-A irradiation (54.6 mW cm^{-1}) and at a temperature of 50 °C.

Synthesis and Characterization of PFPBNT: bis(2-octyldodecyl) 2,2'-(perfluoro-1,4-phenylene)bis(naphtho[1,2-*b*]thiophene-4-carboxylate) (PFPBNT). In a Schlenk tube dried under argon atmosphere were added in sequence, 1,2,4,5-tetrafluorobenzene (55.9 μL, 0.5 mmol, 1 equiv.), 2-octyldodecyl 2-bromonaphtho[1,2-*b*]thiophene-4-carboxylate (588 mg, 1 mmol, 2 equiv.), pivalic acid (25 μL, 2.5 mmol, 5 equiv.), and DMAc (2.5 mL, 0.2 м). Reaction mixture was degassed for 10 min, then Pd(OAc)$_2$ (11 mg, 0.05 mmol, 0.1 equiv.), ^{t}Bu$_2$P(Me)·HBF$_4$ (25 mg, 0.1 mmol, 0.2 equiv.), and K$_2$CO$_3$ (207 mg, 1.5 mmol, 3 equiv.) were added in one portion. Reaction mixture was degassed for another 5 min, warmed to 100 °C and kept at same temperature for 48 h. After TLC monitoring, reaction solvent was removed under reduced pressure and the crude purified by flash chromatography with petroleum ether:DCM (8/2) as eluent. Compound 1 was obtained as brilliant yellow powder in 68% yield (396 mg). ^{1}H NMR (400 MHz, CDCl$_3$) δ: 8.92 (s, 2H), 8.56 (s, 2H), 8.18 (d, J = 7.9 Hz, 2H), 8.01 (d, J = 8.1 Hz, 2H), 7.69 (t, J = 7.5 Hz, 2H), 7.59 (t, J = 7.5 Hz, 2H), 4.41 (d, J = 5.7 Hz, 4H), 1.97–1.88 (m, 2H), 1.61–1.16 (m, 64H), 0.84 (t, J = 7.0, 12H). ^{19}F NMR (376 MHz, CDCl$_3$) δ: −139.3. ^{13}C NMR (101 MHz, CDCl$_3$) δ: 166.4, 145.6, 143.0, 140.1, 134.4, 130.9, 130.2, 130.0, 129. 8, 129.3, 129.1, 127.4, 126. 8, 123.6, 123.5, 113.1, 68.2, 37.4, 31.7, 31.4, 30.7, 29.8, 29.5, 29.2, 26.7, 22.5, 13.9. MALDI-TOF

Computational Modeling of PFPBNT: Atomistic simulations of isolated and aggregated PFPBNT molecules were carried out following a multistep protocol. First, the exploration of potential energy surfaces, particularly relevant in the case of molecular aggregates, was performed by using a semiempirical tight-binding approach; accurate optoelectronic properties were then calculated by using ab initio simulations. In the former case, the GFN2-xTB Hamiltonian[33] was used as "engine" for the search of minimum energy configurations through an automated conformer-rotamer ensemble sampling tool (CREST).[34] In the latter case, (time-dependent) density functional theory simulations were performed in a GTO framework by using the ORCA suite of programs.[35] A detailed description of theoretical methods is reported in the Supporting Information to ensure the full reproducibility of the calculations.

Preparation of PFPBNT/PMMA-LSC in Thin-Film Configuration and LSC-PV Assembly: LSCs were fabricated in thin-film configuration starting from THF solutions of PMMA (20 wt%) with various concentrations of PFPBNT (0.1–17.5 wt% with respect to dry polymer). PFPBNT/PMMA films were obtained by spin coating (1200 rpm for 60 s) onto $5.0 \times 5.0 \times 0.6$ cm^3 N-BK7 glass slabs using a Laurell WS-400BZ-6NPP/LITE instrument. The average coatings thickness was measured by a KLA Tencor P-17 profilometer to be ≈8 µm. Large-area LSC devices ($10.0 \times 10.0 \times 0.6$ cm^3 and $15.0 \times 15.0 \times 0.6$ cm^3) with the same optical density were achieved using doctor-blade technique and commercial soda-lime glass substrates. Also, rectangular-shaped LSCs with dimensions $20.0 \times 5.0 \times 0.6$ cm^3 were fabricated using doctor-blade technique on high-optical-quality N-BK7 glass slabs.

To obtain LSC-PV systems, four monocrystalline silicon solar cells connected in series were coupled to the devices by means of an index matching liquid (Norland IML150, viscosity 100 cps, refractive index ≈1.52), so that two opposite edges of the glass substrates faced the photoactive area of two c-Si solar cells each.

Supporting Information

Supporting Information is available from the Wiley Online Library or from the author.

Acknowledgements

Conflict of Interest

The authors declare no conflict of interest.

Data Availability Statement

The data that supports the findings of this study are available in the supplementary material of this article.

Keywords

[1] a) A. Magrini, G. Lentini, S. Cuman, A. Bodrato, L. Marenco, *Dev. Built Environ.* **2020**, *3*, 100019; b) M. Vasiliev, M. Nur-e-alam, K. Alameh, *Energies* **2019**, *12*, 1080.

[2] a) F. Meinardi, F. Bruni, S. Brovelli, *Nat. Rev. Mater.* **2017**, *2*, 17072; b) G. Kocher-Oberlehner, M. Bardosova, M. Pemble, B. S. Richards, *Sol. Energy Mater. Sol. Cells* **2012**, *104*, 53. c) M. Debije, *Nature* **2015**, *519*, 298; d) C. J. Traverse, R. Pandey, M. C. Barr, R. R. Lunt, *Nat. Energy* **2017**, *2*, 849; e) Y. Li, X. Zhang, Y. Zhang, R. Dong, C. K. Luscombe, *J. Polym. Sci., Part A: Polym. Chem.* **2019**, *57*, 201.

[3] a) A. Goetzberger, W. Greube, *Appl. Phys.* **1977**, *14*, 123. b) A. Goetzberger, *Appl. Phys.* **1978**, *16*, 399.

[4] a) G. Griffini, L. Brambilla, M. Levi, C. Castiglioni, M. Del Zoppo, S. Turri, *RSC Adv.* **2014**, *4*, 9893; b) M. Rafiee, S. Chandra, H. Ahmed, S. J. McCormack, *Opt. Mater.* **2019**, *91*, 212; c) M. J. Currie, J. K. Mapel, T. D. Heidel, S. Goffri, M. A. Baldo, *Science* **2007**, *1*, 2007; d) F. Corsini, E. Tatsi, A. Colombo, C. Dragonetti, C. Botta, S. Turri, G. Griffini, *Nano Energy* **2021**, *80*, 105551.

[5] a) F. Meinardi, Q. A. Akkerman, F. Bruni, S. Park, M. Mauri, Z. Dang, L. Manna, S. Brovelli, *ACS Energy Lett.* **2017**, *2*, 2368; b) H. Zhao, R. Sun, Z. Wang, K. Fu, X. Hu, Y. Zhang, *Adv. Funct. Mater.* **2019**, *29*, 1902262; c) M. Wei, F. P. G. de Arquer, G. Walters, Z. Yang, L. N. Quan, Y. Kim, R. Sabatini, R. Quintero-Bermudez, L. Gao, J. Z. Fan, F. Fan, A. Gold-Parker, M. F. Toney, E. H. Sargent, *Nat. Energy* **2019**, *4*, 197; d) J. Wu, J. Tong, Y. Gao, A. Wang, T. Zhang, H. Tan, S. Nie, *Angew. Chem. Int. Ed.* **2020**, *59*, 7738.

[6] a) L. Zdražil, S. Kalytchuk, K. Holá, M. Petr, O. Zmeškal, Š. Kment, A. L. Rogach, R. Zbořil, *Nanoscale* **2020**, *12*, 6664; b) P. Moraitis, R. E. I. Schropp, W. G. J. H. M. van Sark, *Opt. Mater.* **2018**, *84*, 636; c) Z. Wang, X. Zhao, Z. Guo, P. Miao, X. Gong, *Org. Electron.* **2018**, *62*, 284; d) Y. Li, P. Miao, W. Zhou, X. Gong, X. Zhao, *J. Mater. Chem. A* **2017**, *5*, 21452.

[7] a) F. Purcell-Milton, Y. K. Gun'ko, *J. Mater. Chem.* **2012**, *22*, 16687; b) Y. Zhou, H. Zhao, D. Ma, F. Rosei, *Chem. Soc. Rev.* **2018**, *47*, 5866; c) G. Liu, H. Zhao, F. Diao, Z. Ling, Y. Wang, *J. Mater. Chem. C* **2018**, *6*, 10059; d) V. I. Klimov, T. A. Baker, J. Lim, K. A. Velizhanin, H. McDaniel, *ACS Photonics* **2016**, *3*, 1138; e) K. Wu, H. Li, V. I. Klimov, *Nat. Photonics* **2018**, *12*, 105; f) R. Mazzaro, A. Vomiero, *Adv. Energy Mater.* **2018**, *8*, 1801903.

[8] a) M. G. Debije, P. P. C. Verbunt, *Adv. Energy Mater.* **2012**, *2*, 12; b) B. McKenna, R. C. Evans, *Adv. Mater.* **2017**, *29*, 1606491; c) A. Kaniyoor, B. Mckenna, S. Comby, R. C. Evans, *Adv. Opt. Mater.* **2016**, *4*, 444; d) D. Pintossi, A. Colombo, M. Levi, C. Dragonetti, S. Turri, G. Griffini, *J. Mater. Chem. A* **2017**, *5*, 9067. e) G. Griffini, L. Brambilla, M. Levi, M. Del Zoppo, S. Turri, *Sol. Energy Mater. Sol. Cells* **2013**, *111*, 41.

[9] a) L. R. Wilson, B. C. Rowan, N. Robertson, O. Moudam, A. C. Jones, B. S. Richards, *Appl. Opt.* **2010**, *49*, 1651; b) C. Haines, M. Chen, K. P. Ghiggino, *Sol. Energy Mater. Sol. Cells* **2012**, *105*, 287; c) G. Griffini, *Front. Mater.* **2019**, *6*, 29.

[10] a) M. Yu, R. Huang, J. Guo, Z. Zhao, B. Z. Tang, *PhotoniX* **2020**, *1*, 1; b) J. L. Banal, K. P. Ghiggino, W. W. H. Wong, *Phys. Chem. Chem. Phys.* **2014**, *16*, 25358; c) J. L. Banal, B. Zhang, D. J. Jones, K. P. Ghiggino, W. W. H. Wong, *Acc. Chem. Res.* **2017**, *50*, 49; d) J. L. Banal, J. M. White, K. P. Ghiggino, W. W. H. Wong, *Sci. Rep.* **2014**, *4*, 4635.

[11] a) Y. Hong, J. W. Y. Lam, B. Z. Tang, *Chem. Commun.* **2009**, 4332; b) J. Mei, N. L. C. Leung, R. T. K. Kwok, J. W. Y. Lam, B. Z. Tang, *Chem. Rev.* **2015**, *115*, 11718; c) B. Wang, Z. Yuan, P. Lu, S. Chen, J. W. Y. Lam, Z. Wang, Y. Liu, H. S. Kwok, Y. Ma, B. Z. Tang, *Chem* **2010**, *22*, 2159; d) A. F. Villafiorita-Monteleone, A. Pacini, C. Botta, T. Virgili, A. Forni, E. Cariati, M. Boiocchi, D. Pasini, *Faraday Discuss.* **2017**, *196*, 143.

[12] a) A. Pucci, *Isr. J. Chem.* **2018**, *58*, 837; b) Y. Hong, *Methods Appl. Fluoresc.* **2016**, *4*, 022003; c) F. De Nisi, R. Francischello, A. Battisti, A. Panniello, E. Fanizza, M. Striccoli, X. Gu, N. L. C. Leung, B. Z. Tang, A. Pucci, *Mater. Chem. Front.* **2017**, *1*, 1406; d) F. Gianfaldoni, F. De Nisi, G. Iasilli, A. Panniello, E. Fanizza, M. Striccoli, D. Ryuse, M. Shimizu, T. Biver, A. Pucci, *RSC Adv.* **2017**, *7*, 37302.

[13] a) G. Lyu, J. Kendall, I. Meazzini, E. Preis, S. Bayseç, U. Scherf, S. Clément, R. C. Evans, *ACS Appl. Polym. Mater.* **2019**, *1*, 3039; b) B. Zhang, J. L. Banal, D. J. Jones, B. Z. Tang, K. P. Ghiggino, W. W. H. Wong, *Mater. Chem. Front.* **2018**, *2*, 615.

[14] a) F. Babudri, G. M. Farinola, F. Naso, R. Ragni, *Chem. Commun.* **2007**, 1003; b) A. Nitti, F. Debattista, L. Abbondanza, G. Bianchi, R. Po, D. Pasini, *J. Polym. Sci., Part A: Polym. Chem.* **2017**, *55*, 1601; c) F. Kempe, F. Riehle, H. Komber, R. Matsidik, M. Walter, M. Sommer, *Polym. Chem.* **2020**, *11*, 6928.

[15] a) M. L. Sun, W. S. Zhu, Z. S. Zhang, C. J. Ou, L. H. Xie, Y. Yang, Y. Qian, Y. Zhao, W. Huang, *J. Mater. Chem. C* **2015**, *3*, 94; b) Y. Yu, C. Wang, Y. Wei, Y. Fan, J. Yang, J. Wang, M. Han, Q. Li, Z. Li, *Adv. Opt. Mater.* **2019**, *7*, 1900505; c) H. Zhang, Y. Nie, J. Miao, D. Zhang, Y. Li, G. Liu, G. Sun, X. Jiang, *J. Mater. Chem. C* **2019**, *7*, 3306; d) S. Hayashi, T. Koizumi, *Angew. Chem., Int. Ed.* **2016**, *55*, 2701.

[16] A. Nitti, G. Bianchi, R. Po, T. M. Swager, D. Pasini, *J. Am. Chem. Soc.* **2017**, *139*, 8788.

[17] a) A. Nitti, P. Osw, G. Calcagno, C. Botta, S. I. Etkind, G. Bianchi, R. Po, T. M. Swager, D. Pasini, *Org. Lett.* **2020**, *22*, 3263; b) A. Nitti, P. Osw, M. N. Abdullah, A. Galbiati, D. Pasini, *Synlett* **2018**, *29*, 2577; c) A. Nitti, M. Signorile, G. Bianchi, R. Po, D. Pasini, *J. Org. Chem.* **2016**, *81*, 11035; d) A. Nitti, R. Po, G. Bianchi, D. Pasini, *Molecules* **2017**, *22*, 21.

[18] P. Osw, A. Nitti, M. N. Abdullah, S. I. Etkind, J. Mwaura, A. Galbiati, D. Pasini, *Polymers* **2020**, *12*, 720.

[19] S. Mattiello, A. Sanzone, F. Bruni, M. Gandini, V. Pinchetti, A. Monguzzi, I. Facchinetti, R. Ruffo, F. Meinardi, G. Mattioli, M. Sassi, S. Brovelli, L. Beverina, *Joule* **2020**, *4*, 1988.

[20] a) Y. Tang, B. Z. Tang, *Principles and Applications of Aggregation-Induced Emission*, Springer, Berlin **2018**; b) P. Das, A. Kumar, A. Chowdhury, P. S. Mukherjee, *ACS Omega* **2018**, *3*, 13757; c) J. Geng, K. Li, W. Qin, L. Ma, G. G. Gurzadyan, B. Z. Tang, B. Liu, *Small* **2013**, *9*, 2012.

[21] a) M. Baglan, S. Ozturk, B. Gür, K. Meral, U. Bozkaya, O. A. Bozdemir, S. Atilgan, *RSC Adv.* **2013**, *3*, 15866; b) H. Lu, F. Su, Q. Mei, Y. Tian, W. Tian, R. H. Johnson, D. R. Meldrum, *J. Mater. Chem.* **2012**, *22*, 9890; c) P. Wang, S. Cao, T. Yin, X. L. Ni, *Chin. Chem. Lett.* **2021**, *32*, 1679.

[22] A. Yang, S. Hughes, M. Kuroda, Y. Shiraishi, T. Kobayashi, *Chem. Phys. Lett.* **1997**, *280*, 475.

[23] M. Kasha, H. R. Rawls, M. A. El-Bayoumi, *Pure Appl. Chem.* **1965**, *11*, 371.

[24] G. Griffini, M. Levi, S. Turri, *Renewable Energy* **2015**, *78*, 288.

[25] a) J. Lucarelli, M. Lessi, C. Manzini, P. Minei, F. Bellina, A. Pucci, *Dyes Pigm.* **2016**, *135*, 154; b) R. Mori, G. Iasilli, M. Lessi, A. B. Muñoz-García, M. Pavone, F. Bellina, A. Pucci, *Polym. Chem.* **2018**, *9*, 1168.

[26] E. Tatsi, G. Fortunato, B. Rigatelli, G. Lyu, S. Turri, R. C. Evans, G. Griffini, *ACS Appl. Energy Mater.* **2020**, *3*, 1152.

[27] M. G. Debije, R. C. Evans, G. Griffini, *Energy Environ. Sci.* **2021**, *14*, 293.

[28] a) M. J. Kastelijn, C. W. M. Bastiaansen, M. G. Debije, *Opt. Mater.* **2009**, *31*, 1720; b) B. Zhang, P. Zhao, L. J. Wilson, J. Subbiah, H. Yang, P. Mulvaney, D. J. Jones, K. P. Ghiggino, W. W. H. Wong, *ACS Energy Lett.* **2019**, *4*, 1839; c) H. Li, K. Wu, J. Lim, H. J. Song, V. I. Klimov, *Nat. Energy* **2016**, *1*, 16157.

[29] a) J. ter Schiphorst, M. L. M. K. H. Y. K. Cheng, M. van der Heijden, R. L. Hageman, E. L. Bugg, T. J. L. Wagenaar, M. G. Debije, *Energy Build.* **2020**, *207*, 27; b) C. Yang, D. Liu, R. R. Lunt, *Joule* **2019**, *3*, 2871; c) J. R. Schrecengost, S. D. Bowser, S. W. Weible, J. M. Solomon, L. J. Minner, J. T. Gresh, B. P. Wittmershaus, *Sol. Energy* **2018**, *170*, 132; d) M. G. Debije, J. Teunissen, M. J. Kastelijn, P. P. C. Verbunt, W. M. Bastiaansen, *Sol. Energy Mater. Sol. Cells* **2009**, *93*, 1345.

[30] L. J. Brennan, F. Purcell-Milton, B. McKenna, T. M. Watson, Y. K. Gun'ko, R. C. Evans, *J. Mater. Chem. A* **2018**, *6*, 2671.

[31] A. Nitti, G. Bianchi, R. Po, D. Pasini, *Synthesis* **2019**, *51*, 677.

[32] S. Leyre, E. Coutino-Gonzalez, J. J. Joos, J. Ryckaert, Y. Meuret, D. Poelman, P. F. Smet, G. Durinck, J. Hofkens, G. Deconinck, P. Hanselaer, *Rev. Sci. Instrum.* **2014**, *85*, 123115.

[33] C. Bannwarth, S. Ehlert, S. Grimme, *J. Chem. Theory Comput.* **2019**, *15*, 1652.

[34] a) S. Grimme, *J. Chem. Theory Comput.* **2019**, *15*, 2847; b) P. Pracht, F. Bohle, S. Grimme, *Phys. Chem. Chem. Phys.* **2020**, *22*, 7169.

[35] a) F. Neese, *Wiley Interdiscip. Rev. Comput. Mol. Sci.* **2012**, *2*, 73; b) F. Neese, *Wiley Interdiscip. Rev. Comput. Mol. Sci.* **2018**, *8*, e1327

2100182 (11 of 11)